

This is the accepted manuscript made available via CHORUS. The article has been published as:

## Depth-resolved charge reconstruction at the $\text{LaNiO}_3/\text{CaMnO}_3$ interface

R. U. Chandrasena, C. L. Flint, W. Yang, Arian Arab, S. Nemšák, M. Gehlmann, V. B. Özdöl, F. Bisti, K. D. Wijesekara, J. Meyer-Ilse, E. Gullikson, E. Arenholz, J. Ciston, C. M. Schneider, V. N. Strocov, Y. Suzuki, and A. X. Gray

Phys. Rev. B **98**, 155103 — Published 1 October 2018

DOI: [10.1103/PhysRevB.98.155103](https://doi.org/10.1103/PhysRevB.98.155103)

# Depth-resolved charge reconstruction at the $\text{LaNiO}_3/\text{CaMnO}_3$ interface

R. U. Chandrasena,<sup>1,2</sup> C. L. Flint,<sup>3,4</sup> W. Yang,<sup>1,2</sup> A. Arab,<sup>1,2</sup> S. Nemšák,<sup>5,6</sup> M. Gehlmann,<sup>6</sup>  
V. B. Özdöl,<sup>7</sup> F. Bisti,<sup>8</sup> K. D. Wijesekara,<sup>1,2</sup> J. Meyer-Ilse,<sup>5</sup> E. Gullikson,<sup>5</sup> E. Arenholz,<sup>5</sup>  
J. Ciston,<sup>7</sup> C. M. Schneider,<sup>6</sup> V. N. Strocov,<sup>8</sup> Y. Suzuki,<sup>3,4</sup> and A. X. Gray<sup>1,2,\*</sup>

<sup>1</sup> *Department of Physics, Temple University, 1925 N. 12<sup>th</sup> Street, Philadelphia, Pennsylvania  
19122, USA*

<sup>2</sup> *Temple Materials Institute, Temple University, 1925 N. 12<sup>th</sup> Street, Philadelphia, Pennsylvania  
19122, USA*

<sup>3</sup> *Department of Materials Science and Engineering, Stanford University, Stanford, California  
94305, USA*

<sup>4</sup> *Geballe Laboratory for Advanced Materials, Stanford University, Stanford, California 94305,  
USA*

<sup>5</sup> *Advanced Light Source, Lawrence Berkeley National Laboratory, Berkeley, California 94720,  
USA*

<sup>6</sup> *Peter Grünberg Institut (PGI-6), Forschungszentrum Jülich GmbH, D-52425 Jülich, Germany*

<sup>7</sup> *National Center for Electron Microscopy, Molecular Foundry, Lawrence Berkeley National  
Laboratory, Berkeley, California 94720, USA*

<sup>8</sup> *Swiss Light Source, Paul Scherrer Institute, CH-5232 Villigen, Switzerland*

*\*axgray@temple.edu*

## 1    **Abstract**

2    Rational design of low-dimensional electronic phenomena at oxide interfaces is currently  
3    considered to be one of the most promising schemes for realizing new energy-efficient logic and  
4    memory devices. An atomically-abrupt interface between paramagnetic  $\text{LaNiO}_3$  and  
5    antiferromagnetic  $\text{CaMnO}_3$  exhibits interfacial ferromagnetism, which can be tuned via a  
6    thickness-dependent metal-insulator transition in  $\text{LaNiO}_3$ . Once fully understood, such emergent  
7    functionality could turn this archetypal Mott-interface system into a key building block for the  
8    above-mentioned future devices. Here, we use depth-resolved standing-wave photoemission  
9    spectroscopy in conjunction with scanning transmission electron microscopy and x-ray  
10    absorption spectroscopy, to demonstrate a depth-dependent charge reconstruction at the  
11     $\text{LaNiO}_3/\text{CaMnO}_3$  interface. Our measurements reveal an increased concentration of  $\text{Mn}^{3+}$  and  
12     $\text{Ni}^{2+}$  cations at the interface, which create an electronic environment favourable for the  
13    emergence of interfacial ferromagnetism mediated via the  $\text{Mn}^{4+}\text{-Mn}^{3+}$  ferromagnetic double  
14    exchange and  $\text{Ni}^{2+}\text{-O-Mn}^{4+}$  superexchange mechanisms. Our findings suggest a new strategy for  
15    designing functional Mott oxide heterostructures by tuning the interfacial cation characteristics  
16    via controlled manipulation of thickness, strain, and ionic defect states.

1 Multifunctional complex-oxide heterostructures have been identified as candidate materials  
2 systems that may enable the coupling of electronic logic with magnetic memory and lead to the  
3 next-generation of spintronic devices [1-5]. Among the many complex-oxide heterostructures  
4 studied to date, there has been a class of heterostructures where the interfaces give rise to  
5 functional properties not observed in the constituent materials [6]. With many such emergent  
6 properties, ranging from interfacial metallicity [7-9] to interfacial superconductivity [10,11],  
7 there has been only a handful of successful efforts demonstrating new magnetic ground states at  
8 interfaces [12,13]. One such example is the  $\text{LaNiO}_3/\text{CaMnO}_3$  system where ferromagnetic  
9 ground state emerges at the interface, although  $\text{LaNiO}_3$  is a paramagnetic metal and  $\text{CaMnO}_3$  is  
10 an antiferromagnetic insulator in the bulk [13-15].

11 The emergence of interfacial ferromagnetism in the  $\text{LaNiO}_3/\text{CaMnO}_3$  system has been  
12 attributed to two distinct mechanisms: a  $\text{Mn}^{4+}\text{-Mn}^{3+}$  double exchange interaction in the  
13 interfacial  $\text{CaMnO}_3$  layer and a  $\text{Ni}^{2+}\text{-O-Mn}^{4+}$  superexchange interaction at the interface between  
14 the  $\text{LaNiO}_3$  and  $\text{CaMnO}_3$  [13-15]. The relative importance of the two mechanisms depends on  
15 the thickness of the individual layers due to a thickness-dependent metal-insulator transition in  
16 the  $\text{LaNiO}_3$  layer [16-18]. The transition, which occurs in the ultrathin (few-unit-cell) limit,  
17 determines which is the dominant mechanism for the mediation of the ferromagnetic coupling.  
18 Such tunability provides an ideal platform for studying fundamental interactions leading to  
19 emergent magnetism at oxide interfaces and makes this heterostructure a potential candidate for  
20 the above-mentioned devices. [12,19,20].

21 Both of the above mentioned mechanisms require an interfacial charge reconstruction,  
22 which results in the presence of the transition-metal cations with the valence states other than the  
23 formal valence state of the stoichiometric compounds ( $\text{LaNi}^{3+}\text{O}_3$  and  $\text{CaMn}^{4+}\text{O}_3$ ). Such charge

reconstruction, resulting in the formation of off-stoichiometric cations ( $\text{Ni}^{2+}$  and  $\text{Mn}^{3+}$ ) at the interface, can be explained in terms of the charge leakage from  $\text{LaNiO}_3$  to  $\text{CaMnO}_3$  [13-15], as well as the presence of oxygen vacancies driven to the interface by polar compensation [21-24]. Both scenarios are plausible in the  $\text{LaNiO}_3/\text{CaMnO}_3$  heterostructures. Specifically, in metallic superlattices with near- and above-critical  $\text{LaNiO}_3$  thicknesses, leakage of itinerant Ni  $3d$   $e_g$  electrons into the interfacial  $\text{CaMnO}_3$  layer is expected to reduce the valence state of some of the interfacial Mn cations from  $4+$  to  $3+$ , leading to the emergence of interfacial ferromagnetism mediated by the  $\text{Mn}^{4+}\text{-Mn}^{3+}$  double exchange interaction [13-15,25]. This scenario has been theoretically predicted and discussed in-depth in prior experimental studies [13-15] and could explain the observed link between the thickness-dependent metal-insulator transition in ultrathin  $\text{LaNiO}_3$  and the observed suppression of ferromagnetism in the superlattices with near- and below-critical-thickness  $\text{LaNiO}_3$  layers (see Fig. 2 in Ref. [15]). In superlattices with thinner  $\text{LaNiO}_3$ , which is closer to the metal-insulator transition and hence more resistive transport properties,  $\text{Ni}^{2+}\text{-O-Mn}^{4+}$  superexchange interaction (made possible by oxygen vacancies driven to the interface) has been identified as the source of the interfacial ferromagnetism [14,15]. On the other hand, oxygen vacancies have also been observed in coherently strained epitaxial  $\text{CaMnO}_3$  [21] and  $\text{LaNiO}_3$  [22-24] and, in some cases, have been both predicted and observed to segregate at the interfaces due to polar energetics at the interface [22,23].

Gaining a clear picture of the depth-dependent evolution of materials' electronic properties, valence states, and charge redistribution across the interface is therefore required to determine the roles of double exchange and superexchange interactions in the emergence of the observed interfacial ferromagnetism in this system. Thus, here, we used a combination of depth-resolved soft x-ray standing-wave photoemission spectroscopy (SW-XPS), x-ray absorption spectroscopy

(XAS), and scanning transmission electron microscopy (STEM) to selectively probe the interface electronic structure and valence states of the relevant transition metal cations (Mn and Ni). Our results reveal an increased concentration of  $\text{Mn}^{3+}$  and  $\text{Ni}^{2+}$  cations at the  $\text{LaNiO}_3/\text{CaMnO}_3$  interface, indicating the coexistence of competing  $\text{Mn}^{3+}$ - $\text{Mn}^{4+}$  double exchange with  $\text{Ni}^{2+}$ -O- $\text{Mn}^{4+}$  superexchange interactions that give rise to emergent interfacial ferromagnetism.

For this study, high-quality epitaxial  $[4 \text{ u.c. } \text{LaNiO}_3 / 4 \text{ u.c. } \text{CaMnO}_3] \times 15$  superlattice was synthesized on top of a single-crystalline  $\text{LaAlO}_3$  (001) substrate using pulsed laser deposition. Layer-by-layer growth was monitored in-situ using reflection high-energy electron diffraction. After deposition, coherent epitaxy, crystallinity and layering of the superlattice was verified using ex-situ x-ray diffraction spectroscopy (XRD), soft x-ray reflectivity (SXR), as well as STEM (see Fig. 1). Bulk magnetization and electronic transport measurements, carried out by us in a prior study on similar samples [15], revealed a ferromagnetic signal ( $0.3 \mu\text{B}/\text{Int.Mn}$  at 10 K) and temperature-dependent resistivity ( $4 \times 10^{-4} \text{ Ohm-cm}$  at 10 K), which is consistent with the onset of metallicity in  $\text{LaNiO}_3$ . More details regarding the deposition process and sample characterization can be found in Ref. [15].

A high-angular-resolution ( $<0.01^\circ$ ) XRD  $2\theta$ - $\theta$  spectrum in Fig. 1(a), recorded using a Bruker D8 Discover diffractometer, shows well-resolved superlattice (SL) period thickness fringes and Bragg peaks, thus attesting to the high quality and precise control of the SL synthesis. A high-angular-resolution ( $<0.01^\circ$ ) SXR spectrum (see inset), recorded at the Calibration and Standards beamline 6.3.2 of the Advanced Light Source (LBNL), confirms the presence and the angular position of the SL Bragg peak in the soft x-ray regime at the photon energy used for the SX-XPS measurements described below.

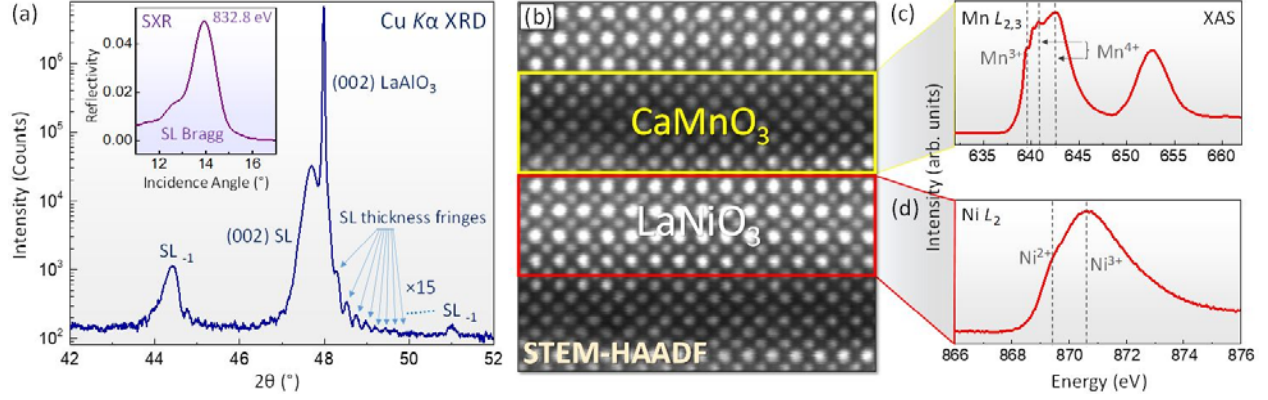


FIG. 1. (a) XRD  $2\theta$  spectrum around the  $\text{LaAlO}_3$  (002) peak shows clearly-resolved SL thickness fringes, as well as the first-order SL Bragg peaks. Inset shows a synchrotron-based SXR spectrum (at  $h\nu = 832.8$  eV) of the first-order superlattice Bragg peak in the soft x-ray regime. (b) High-resolution STEM-HAADF cross sectional image of the superlattice sample showing a typical atomically-abrupt  $\text{LaNiO}_3/\text{CaMnO}_3$  interface. (c) and (d) The XAS spectra probing the  $\text{CaMnO}_3$  layer at the Mn  $L_{2,3}$  absorption edges (c), and the  $\text{LaNiO}_3$  layer at the Ni  $L_2$  edge (d) reveal mixed valence states for the Mn (3+ and 4+) and Ni (2+ and 3+) cations in the respective layers.

At the atomic level, the high-angle annular dark-field (HAADF) STEM image in Fig. 1(b), recorded using the aberration-corrected TEAM I microscope at the National Center for Electron Microscopy Facility of the Molecular Foundry (LBNL), shows several typical atomically-abrupt interfaces between  $\text{LaNiO}_3$  and  $\text{CaMnO}_3$ . The A-site (La and Ca) atomic columns can be easily differentiated due to the high atomic number contrast, with the heavier cations (La) appearing brighter. The interfacial layers show some fluctuations in atomic column intensity of the A-sites, suggesting that the interfacial mixing is confined to a single unit cell, consistent with a prior study on similar samples [13].

The high-resolution (100 meV) XAS spectra of the Mn  $L_{2,3}$  and Ni  $L_2$  absorption edges, recorded in the total electron yield (TEY) detection mode at the Magnetic Spectroscopy beamline of the Advanced Light Source (LBNL) [26], reveal fine spectral features attributed to the  $\text{Mn}^{3+}$  and  $\text{Mn}^{4+}$  cations at 640 eV and 643 eV, respectively [Fig. 1(c)] [21]; as well as the

1  $\text{Ni}^{2+}$  (869.5 eV) and  $\text{Ni}^{3+}$  (870.5 eV) peak components at the Ni  $L_2$  edge [Fig. 1(d)] [27-29]. The  
2 data thus suggest a mixture of  $\text{Mn}^{3+}$  and  $\text{Mn}^{4+}$  cations originating in the  $\text{CaMnO}_3$  layer and a  
3 mixture of  $\text{Ni}^{2+}$  and  $\text{Ni}^{3+}$  cations originating in the  $\text{LaNiO}_3$  layer. However, XAS-TEY is a depth-  
4 averaging spectroscopic technique with a typical probing depth of 5 nm [30,31], and thus does  
5 not provide a depth-resolved valence-state profile of the structure with sufficient resolution.

6 Thus, in order to selectively probe the electronic structure and valence-states of the Mn and  
7 Ni cations at the  $\text{LaNiO}_3/\text{CaMnO}_3$  interface, we have carried out soft x-ray SW-XPS  
8 measurements at the high-resolution ADRESS beamline of the Swiss Light Source [32,33]. The  
9 SX-ARPES end station at the ADRESS beamline was equipped with a SPECS PHOIBOS-150  
10 hemispherical electrostatic analyzer and a six-axis cryogenic manipulator, allowing for optimal  
11 alignment of the sample and high-precision angle-resolved standing-wave measurements. The  
12 above mentioned measurements were accomplished by setting-up an x-ray standing-wave field  
13 within the periodic  $[4 \text{ u.c. } \text{LaNiO}_3 / 4 \text{ u.c. } \text{CaMnO}_3] \times 15$  superlattice sample, which in first-order  
14 Bragg reflection acted as the standing-wave generator [see Fig. 2(a)]. The antinodes of the  
15 standing wave were moved vertically through the sample by scanning (rocking) the x-ray  
16 incidence angle [34,35]. The sample temperature was set at 30 K.

17 The photon energy of 832.8 eV, just below the La  $3d_{5/2}$  absorption threshold, was used to  
18 maximize the x-ray reflectivity of the superlattice, which in-turn enhanced the standing-wave  
19 modulation amplitude. In preparation for the experiment, energy-dependent SXR measurements  
20 were carried out to fine-tune the experimental parameters, such as the optimal photon energy and  
21 the angular range for the x-ray incidence [see inset in Fig. 1(a)].

22 Core-level photoemission intensities from every constituent element of the superlattice (La  
23  $4d$ , Ni  $3p$ , Ca  $2p$ , Mn  $3s$ , O  $1s$  and C  $1s$ ) were recorded as a function of grazing incidence angle



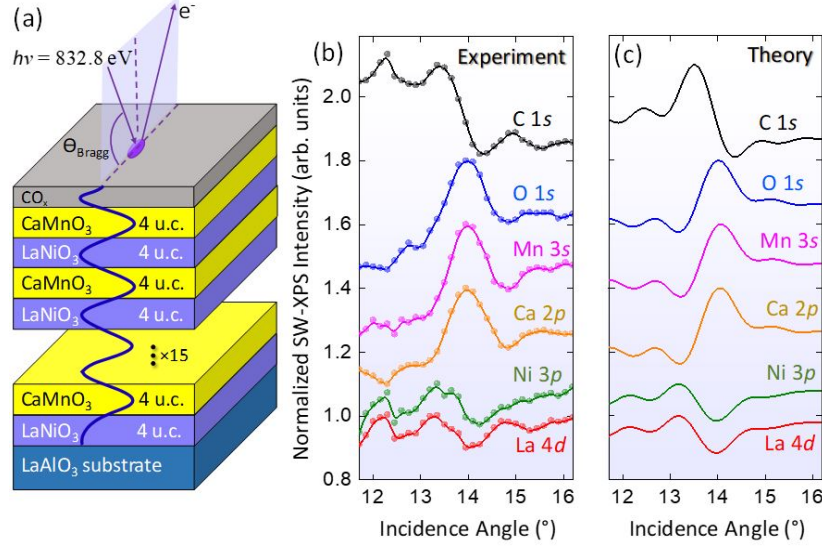


FIG. 2. (a) Schematic diagram of the investigated superlattice structure consisting of fifteen  $\text{LaNiO}_3/\text{CaMnO}_3$  bilayers, grown epitaxially on a single-crystal  $\text{LaAlO}_3$  substrate, with each bilayer consisting of 4 unit cells of  $\text{LaNiO}_3$  and 4 unit cells of  $\text{CaMnO}_3$ . An excitation photon energy of 832.8 eV, corresponding to the onset of the  $\text{La } 3d_{5/2}$  absorption threshold, was utilized for the photoemission experiments to enhance the standing-wave modulation amplitude at the Bragg condition. (b) Experimental core-level photoemission intensity rocking curves for all elements in the superlattice and (c) best theoretical fits to the data.

1 from  $11.7^\circ$  to  $16.2^\circ$  [see Fig. 2(b)] and self-consistently fitted using an x-ray optical theoretical  
2 code [36], which accounts for the differential photoelectric cross-section as well as the inelastic  
3 mean-free paths of photoelectrons inside the sample. Only the thicknesses of the  $\text{CaMnO}_3$  and  
4  $\text{LaNiO}_3$  layers and the interdiffusion between them were allowed to vary in the model. The x-ray  
5 optical constants needed for the calculations were obtained via XAS and Kramer-Kronig analysis  
6 [34]. Fig. 2(c) shows the best theoretical fits to the experimental data, exhibiting excellent  
7 agreement in terms of the amplitudes, relative phases and shapes. Surface-adsorbed  $\text{CO}_x$   
8 contaminate from the exposure to atmosphere provides an excellent depth reference (black  
9 spectrum), thus further constraining the fitting and the calculations.

1 A detailed structure of the topmost layers derived from the experiment, as well as the  
2 simulated intensity of the x-ray standing-wave electric field ( $E^2$ ) as a function of depth inside the  
3 sample and of x-ray incidence angle, are shown in Fig. 3(a) and were obtained by using the set of  
4 best-fit parameters. Resultant thicknesses of the 4 u.c.-thick layers of LaNiO<sub>3</sub> (15.55 Å) and  
5 CaMnO<sub>3</sub> (14.80 Å) are consistent with the unit cell thicknesses of 3.89 Å (LaNiO<sub>3</sub>) and 3.73 Å  
6 (CaMnO<sub>3</sub>), reported previously in the literature [37-39].

7 The  $E^2$  profile simulation shown in Fig. 3(a) indicates that at lower incidence angles  
8 (yellow vertical line at ~13.3°) the two antinodes of the standing wave highlight predominantly  
9 the top and the bottom interfaces of the CaMnO<sub>3</sub> film (regions marked with letters 'a'), while the  
10 middle 'bulk-like' section of the film resides in the dark region (SW node). With increasing  
11 incidence angle, the top antinode propagates downward into the CaMnO<sub>3</sub> layer spreading over  
12 almost the entire 4 unit-cells at around 14.4° (marked with another yellow vertical line) with the  
13 maximum intensity at approximately the center of the layer (region marked with letter 'b'). Such  
14 contrasting angle-dependent depth distribution of the probing x-ray  $E$ -field intensities within the  
15 sample enables clear differentiation between the bulk-like and interface-like species of Mn in the  
16 CaMnO<sub>3</sub> layer, as well as a particular sensitivity to the interface-like Ni in the LaNiO<sub>3</sub> buried  
17 layer. Importantly, the simulation results indicate that the standing-wave contrast within the  
18 topmost layers of the sample is strong, reaching maximum difference of approximately 53%  
19 between the values of  $E^2$  in the nodes and antinodes of the SW [see the color scale in Fig. 3(a)].  
20 Additional line-cuts, showing  $E$ -field intensity profiles at several key incidence angles are shown  
21 in Fig. S1 in the Supplemental Material section [40].

22 In order to determine the valence-state profiles of the key cations, we examine the  
23 lineshapes of the Mn 3s and Ni 3p core-level spectra at the x-ray grazing incidence angles

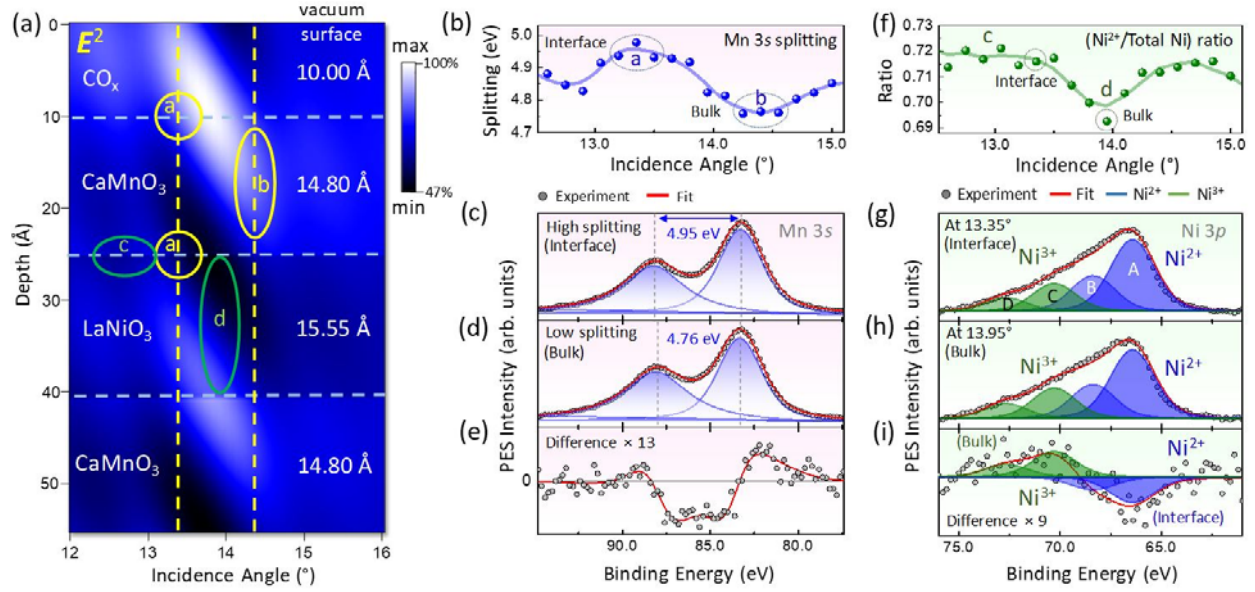


FIG. 3. (a) Simulated intensity of the x-ray standing-wave electric field ( $E^2$ ) inside the superlattice as a function of depth (vertical axis) and x-ray grazing incidence angle (horizontal axis). Calculated layer thicknesses shown on the right are consistent with the  $4\times$  multiples of the  $\text{LaNiO}_3$  and  $\text{CaMnO}_3$  unit-cell constants reported in the literature [37-39]. (b) Depth dependent evolution of the Mn 3s multiplet splitting (in eV) as a function of the x-ray grazing incidence angle. (c) and (d) Mn 3s core-level photoemission spectra recorded in the interface-sensitive ( $\sim 13.3^\circ$ ) and bulk-sensitive ( $\sim 14.4^\circ$ ) experimental geometries, respectively. (e) Difference spectrum obtained by subtracting the spectrum obtained at  $\sim 13.3^\circ$  (c) from that obtained at  $\sim 14.4^\circ$  (d). (f) Plot of the relative  $\text{Ni}^{2+}$  peak(s) intensity as a function of x-ray grazing incidence angle. (g) and (h) Ni 3p core-level photoemission spectra recorded at  $\sim 13.35^\circ$  and  $\sim 13.95^\circ$  respectively. (i) 'Bulk - interface' difference spectrum obtained by subtracting the spectrum obtained at  $\sim 13.35^\circ$  (g) from that obtained at  $\sim 13.95^\circ$  (h).

1 corresponding to the interface-sensitive and bulk-sensitive standing-wave configurations.  
2 Conventional photoemission spectra for typical bulk-like stoichiometric or near-stoichiometric  
3  $\text{CaMnO}_3$  and  $\text{LaNiO}_3$  thin films are provided for reference in the Supplemental Material section  
4 (Fig. S2).

5 Fig. 3(b) depicts the depth-dependent evolution of the Mn 3s core-level multiplet splitting  
6 (in eV) as function of x-ray incidence angle. The magnitude of the 3s splitting decreases  
7 monotonically with the increase of the formal valency of the Mn cation [41,42], and is thus often

used as a reliable and highly sensitive experimental observable for determining the Mn valence state [21,42]. In the  $\text{CaMnO}_3$ -interface sensitive experimental geometry, at the x-ray incidence angles between  $13.2^\circ$  and  $13.5^\circ$  (corresponding to region ‘a’ in the sample), the average splitting is estimated to be 4.95 eV, after self-consistent Shirley-background subtraction and peak-fitting (see Fig. 3(c)). This value of splitting corresponds to the formal Mn valency of approximately +3.4 [41], thus suggesting a mixture of  $\text{Mn}^{+3}$  and  $\text{Mn}^{+4}$  cations, with predominantly  $\text{Mn}^{3+}$  ion content at the interface.

For higher x-ray incidence angles, as the SW antinode propagates toward the center of the  $\text{CaMnO}_3$  layer [as shown in Fig. 3(a)], the Mn 3s splitting gradually decreases, reaching a value of 4.76 eV [see Fig. 2(c)] in the  $\text{CaMnO}_3$ -bulk sensitive geometry, at the incidence angle of  $\sim 14.4^\circ$  (corresponding to region ‘b’ in the sample). For this magnitude of the 3s splitting, formal valency of the Mn cations is estimated to be approximately +3.6 [41], which suggests an increase of the  $\text{Mn}^{+4}$  ion concentration (as in stoichiometric  $\text{CaMnO}_3$ ) toward the bulk of the layer.

The difference spectrum in Fig. 3(e), comparing Mn 3s spectra in the interface-sensitive and bulk-sensitive experimental geometries, exhibits a lineshape that is typical of the increasing splitting, with positive incursions at 82 eV and 88 eV and a negative dip emerging between the two separated multiplet components. The observed change in the Mn 3s splitting (190 meV) is approximately a factor of two larger as compared to the total experimental energy resolution ( $\sim 100$  meV).

Conventional surface-sensitive XPS spectrum recorded with the same photon energy but away from the Bragg condition shows that the value of the Mn 3s splitting measured near the surface is 4.81 eV, which is close to the bulk-like value of 4.76 eV (see Fig. S3 in the Supplemental Material section). The splitting increases significantly to 4.95 eV (becomes more

Mn<sup>3+</sup>-like) only when the additional standing-wave intensity highlights the bottom (buried) interface with LaNiO<sub>3</sub>.

In summary, our experimental SW-XPS results, in conjunction with x-ray optical modeling, indicate an increased concentration of Mn<sup>3+</sup> cations in the interfacial regions of the CaMnO<sub>3</sub> film. Evidence of such charge reconstruction has been observed indirectly in prior studies using depth-averaging techniques [13,15]. There are two possible sources of Mn<sup>3+</sup> at the interfaces: the leakage of itinerant electrons from the LaNiO<sub>3</sub> to the CaMnO<sub>3</sub> and the segregation of oxygen vacancies in CaMnO<sub>3</sub> to the interfaces. The temperature-dependent resistivity data suggests the onset of metallicity in superlattices with 4 u.c.-thick LaNiO<sub>3</sub> layers, with increasingly lower resistivities in superlattices with thicker LaNiO<sub>3</sub> layers (*e.g.* 6 - 8 u.c. – see Fig. 2 in Ref. [15]), and therefore the mechanism of the leakage of itinerant electrons from LaNiO<sub>3</sub> into the first CaMnO<sub>3</sub> layer is the likely explanation in our superlattice. With increasing metallicity of the LaNiO<sub>3</sub> layers, the emergent interfacial ferromagnetism is dominated by the Mn<sup>4+</sup>-Mn<sup>3+</sup> double exchange interaction mediated by the leakage of the itinerant electrons and not Ni<sup>2+</sup>-O-Mn<sup>4+</sup> superexchange interactions.

Mn<sup>3+</sup>-Mn<sup>4+</sup> disproportionation at the interface is predicted to stabilize Mn<sup>4+</sup>-Mn<sup>3+</sup> double-exchange ferromagnetism, various signatures of which have been observed via bulk magnetometry, polarization-dependent XAS, and polarized neutron reflectometry (PNR) [13,15]. The latter technique provides a depth-resolved profile of magnetization in the superlattice and has shown that ferromagnetism in the CaMnO<sub>3</sub> film is confined to one unit-cell at the interface with LaNiO<sub>3</sub>, in agreement with our conclusions [13]. Our depth-resolved SW-XPS results thus provide a direct experimental link between the emergent magnetic and electronic interfacial

properties and represent strong evidence to support the model of  $\text{Mn}^{4+}$ - $\text{Mn}^{3+}$  double-exchange-mediated ferromagnetism in the  $\text{LaNiO}_3/\text{CaMnO}_3$  superlattices.

The emergence of interfacial ferromagnetism mediated by the  $\text{Ni}^{2+}$ -O- $\text{Mn}^{4+}$  superexchange interactions requires the presence of off-stoichiometric  $\text{Ni}^{2+}$  cations at the interface. In Figs. 3(f)-(i), we show the depth-dependent evolution of several features of the Ni  $3p$  core-level peak, which have been used in numerous prior studies to determine the Ni valence state in  $\text{LaNiO}_3$  [43,44] and related compounds [45]. We label these components A-D in Fig. 3(g), in accordance with the convention used by Qiao *et al.* [see Fig. S2(b) from Ref. [43]]. Features A and C can be assigned to the  $\text{Ni}^{2+} 3p_{3/2}$  and  $\text{Ni}^{3+} 3p_{3/2}$ , respectively; while B and D are their  $3p_{1/2}$  counterparts [43].

It is immediately apparent from Figs. 3(g)-(h) that the  $\text{Ni}^{2+}$  components (A and B) are more intense, as compared to the  $\text{Ni}^{3+}$  peaks (C and D). However, it is important to note that due to the inelastic attenuation of the photoelectrons in the buried  $\text{LaNiO}_3$  layer, at the photon energy of 832.8 eV we are mostly sensitive to the top-most 'interface-like' region of the film. In fact, with the inelastic mean-free path estimated at  $\sim 15$  Å [46], intensity of the photoemission signal from the central 'bulk-like' region of the film is diminished by approximately 40%, compared to the photoemission signal originating from the top  $\text{LaNiO}_3/\text{CaMnO}_3$  interface [46,47]. Thus, from the first evaluation of the  $3p$  spectral lineshapes in Figs. 3(g)-(h), we can conclude that the interface region of the buried  $\text{LaNiO}_3$  film contains a significant concentration of the  $\text{Ni}^{2+}$  cations. For measurements carried out at incidence angles that are sufficiently far away from the Bragg condition to ensure almost uniform illumination of the film ( $12.5^\circ$ - $13.3^\circ$ , or region 'c' in Fig. 3(a)), the relative intensity ratio (RIR) of the  $\text{Ni}^{2+}$  peak components to the total  $3p$  intensity is estimated to be  $\sim 0.71$  [see Fig. 3(f)].

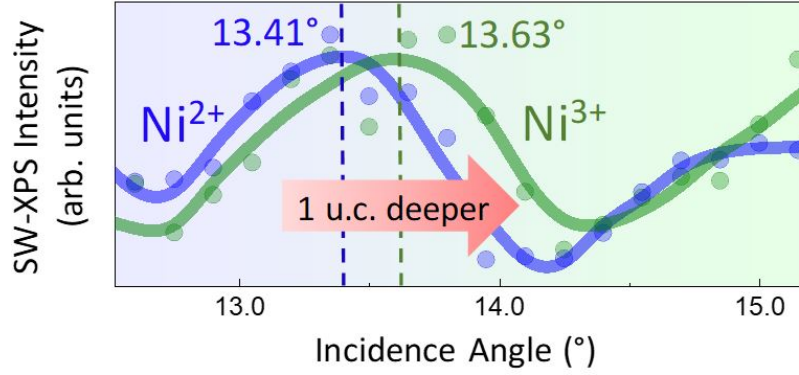


FIG. 4. Individual standing-wave rocking-curve modulations for the  $\text{Ni}^{2+}$  (blue) and  $\text{Ni}^{3+}$  (green) components of the Ni 3*p* core-level spectrum shown in Fig. 3(g). A relative shift of approximately  $+0.3^\circ$  of the  $\text{Ni}^{3+}$  component with respect to the  $\text{Ni}^{2+}$  component corresponds to a  $3.2 \text{ \AA}$  ( $\sim 1 \text{ u.c.}$ ) increase in the depth position of the SW probe inside of the  $\text{LaNiO}_3$  layer. Circles correspond to experimental data and solid lines correspond to guides-to-the-eye obtained via polynomial fitting of the data.

Remarkably, in the Bragg condition, a SW node (dark spot) appears at the  $\text{LaNiO}_3/\text{CaMnO}_3$  interface at  $\sim 13.35^\circ$  and propagates into the  $\text{LaNiO}_3$  layer, thus suppressing the signal from the interface with a maximum effect at approximately  $14.0^\circ$  (region 'd' in Fig. 3(a)). Within the same angular range of  $\sim 13.3^\circ$ - $14.0^\circ$ , an antinode (bright spot) appears in the central region of the film, thus enhancing the signal from the 'bulk-like'  $\text{LaNiO}_3$ . Our data in Fig. 3(e) reveals that such enhancement of the 'bulk-like' signal (and simultaneous suppression of the 'interface-like' signal) results in a significant drop of the  $\text{Ni}^{2+}$  RIR and an increase in the relative  $\text{Ni}^{3+}$  peak intensities. A difference plot, comparing Ni 3*p* spectra in the interface-sensitive and bulk-sensitive experimental geometries highlights this depth-dependent disproportionation of the Ni valence states [Fig. 3(i)].

An effective way of confirming the above described depth-dependent disproportionation of the Ni species within the  $\text{LaNiO}_3$  layer is to compare the lineshapes of the rocking curves (RC) for the  $\text{Ni}^{2+}$  (A+B - blue) and  $\text{Ni}^{3+}$  (C+D - green) individual components. Fig. 4 reveals a clear



1 shift to a higher grazing incidence angle of the entire  $\text{Ni}^{3+}$  component RC, relative to the  $\text{Ni}^{2+}$   
2 RC. Such angular shift (estimated at approximately  $0.3^\circ$ ) corresponds to a  $\sim 3.2$  Å (about 1 unit-  
3 cell) increase in the depth position of the SW probe inside of the  $\text{LaNiO}_3$  layer. Thus, the  
4 difference in the angular characteristics of the rocking curves in Fig. 4 suggests that the  $\text{Ni}^{2+}$   
5 components of the Ni 3*p* spectrum originate mainly from the interfacial region with  $\text{CaMnO}_3$ ,  
6 while the  $\text{Ni}^{3+}$  signal comes mainly from the deeper 'bulk-like'  $\text{LaNiO}_3$  layers.

7 Evidence of such interfacial charge redistribution has been observed in a prior combined  
8 XAS and resonant soft x-ray scattering study on similar superlattices [15] and is consistent with  
9 the polar compensation picture [15,22], wherein polar mismatch at the  $\text{LaNiO}_3/\text{CaMnO}_3$   
10 interface leads to interfacial  $\text{Ni}^{2+}$  cations in the polar  $\text{LaNiO}_3$  layer through the formation of  
11 oxygen vacancies. The ensuing interaction between the interfacial  $\text{Ni}^{2+}$  and adjacent  $\text{Mn}^{4+}$  on the  
12  $\text{CaMnO}_3$  side of the interface is predicted to stabilize the ferromagnetic ground state via the  
13 superexchange mechanism [48,49]. Our depth-resolved SW-XPS results support this model and  
14 suggest that this interaction is likely confined to a narrow (1 unit-cell) region at the interface.

15 In conclusion, in this study we used SW-XPS in conjunction with x-ray optical modeling to  
16 determine the valence-state profile of the Mn and Ni cations at an atomically-abrupt epitaxial 4  
17 u.c.  $\text{LaNiO}_3$  / 4 u.c.  $\text{CaMnO}_3$  interface - a potential building-block for next-generation spintronic  
18 devices. By looking at the depth-resolved evolution of the spectral lineshapes of the Mn 3*s* and  
19 Ni 3*p* core levels, we observed an increased concentration of  $\text{Mn}^{3+}$  and  $\text{Ni}^{2+}$  cations at the buried  
20 interface. Concomitantly, the 'formal valence' cations ( $\text{Mn}^{4+}$  and  $\text{Ni}^{3+}$ ) were shown to be more  
21 abundant in the 'bulk-like' regions of the respective films. The observed depth-dependent charge  
22 redistribution creates an electronic environment favorable for the emergence of interfacial  
23 ferromagnetism mediated via the  $\text{Mn}^{4+}\text{-Mn}^{3+}$  ferromagnetic double exchange and  $\text{Ni}^{2+}\text{-O-Mn}^{4+}$



superexchange mechanisms. The competition between these two mechanisms can be influenced by tuning the thickness of the  $\text{LaNiO}_3$  layer, which undergoes a metal-insulator transition in the ultrathin limit ( $<4$  u.c.), resulting in the thickness-dependent controllability of the magnetic moment at the interface as demonstrated in a prior study [15].

A.X.G., R.U.C., W.Y. and A.A. acknowledge support from the U.S. Army Research Office, under Grant No. W911NF-15-1-0181. C.L.F. and Y.S. acknowledge support from the U.S. Department of Energy, Director, Office of Science, Office of Basic Energy Sciences, Division of Materials Sciences and Engineering, under Contract No. DESC0008505. Work at the Advanced Light Source and Molecular Foundry user facilities was supported by the Office of Science, Office of Basic Energy Sciences, of the U.S. Department of Energy under Contract No. DE-AC02-05CH11231. F.B. acknowledges funding by the Swiss National Science Foundation Grant No. 200021\_146890 and by the European Community's Seventh Framework Programme (FP7/2007-2013) Grant No. 290605 (PSI-FELLOW/COFUND).

## REFERENCES

- [1] R. Ramesh and N. A. Spaldin, Nat. Mater. **6**, 21 (2007).
- [2] J. M. Rondinelli, M. Stengel, and N. A. Spaldin, Nat. Nanotechnol. **3**, 46 (2007).
- [3] M. Bibes, J. E. Villegas, and A. Barthélémy, Adv. Phys. **60**, 5 (2011).
- [4] P. Zubko, S. Gariglio, M. Gabay, P. Ghosez, and J.-M. Triscone, Annu. Rev. Condens. Matter Phys. **2**, 141 (2011).
- [5] S. Fusil, V. Garcia, A. Barthélémy, and M. Bibes, Annu. Rev. Mater. Res. **44**, 91 (2014).
- [6] H. Y. Hwang, Y. Iwasa, M. Kawasaki, B. Keimer, N. Nagaosa, and Y. Tokura, Nat. Mater. **11**, 103 (2012).
- [7] P. Moetakef, J. Y. Zhang, A. Kozhanov, B. Jalan, R. Seshadri, S. J. Allen, and S. Stemmer, Appl. Phys. Lett. **99**, 232116 (2011).

- [8] A. Ohtomo and H. Y. Hwang, *Nature* **427**, 423 (2004).
- [9] A. Ohtomo, D. A. Muller, J. L. Grazul, and H. Y. Hwang, *Nature* **419**, 378 (2002).
- [10] A. Gozar, G. Logvenov, L. F. Kourkoutis, A. T. Bollinger, L. A. Giannuzzi, D. A. Muller, and I. Bozovic, *Nature* **455**, 782 (2008).
- [11] N. Reyren, S. Thiel, A. D. Caviglia, L. Fitting Kourkoutis, G. Hammerl, C. Richter, C. W. Schneider, T. Kopp, A.-S. Rüetschi, D. Jaccard, M. Gabay, D. A. Muller, J.-M. Triscone, and J. Mannhart, *Science* **317**, 1196 (2007).
- [12] K. S. Takahashi, M. Kawasaki, and Y. Tokura, *Appl. Phys. Lett.* **79**, 1324 (2001).
- [13] A. J. Grutter, H. Yang, B. J. Kirby, M. R. Fitzsimmons, J. A. Aguiar, N. D. Browning, C. A. Jenkins, E. Arenholz, V. V. Mehta, U. S. Alaun, and Y. Suzuki, *Phys. Rev. Lett.* **111**, 087202 (2013).
- [14] C. L. Flint, A. Vailionis, H. Zhou, H. Jang, J. S. Lee, and Y. Suzuki, *Phys. Rev. B* **96**, 144438 (2017).
- [15] C. L. Flint, H. Jang, J. S. Lee, A. T. N'Diaye, P. Shafer, E. Arenholz, and Y. Suzuki, *Phys. Rev. Materials* **1**, 024404 (2017).
- [16] R. Scherwitzl, S. Gariglio, M. Gabay, P. Zubko, M. Gibert, and J. M. Triscone, *Phys. Rev. Lett.* **106**, 246403 (2011).
- [17] D. P. Kumah, A. S. Disa, J. H. Ngai, H. Chen, A. Malashevich, J. W. Reiner, S. Ismail-Beigi, F. J. Walker, and C. H. Ahn, *Adv. Mater.* **26**, 1935 (2014).
- [18] S. Middey, J. Chakhalian, P. Mahadevan, J. W. Freeland, A. J. Millis, and D. D. Sarma, *Annu. Rev. Mater. Res.* **46**, 305 (2016).
- [19] J. Hoffman, I. C. Tung, B. B. Nelson-Cheeseman, M. Liu, J. W. Freeland, and A. Bhattacharya, *Phys. Rev. B* **88**, 144411 (2013).
- [20] A. Bhattacharya and S. J. May, *Annu. Rev. Mater. Res.* **44**, 65 (2014).
- [21] R. U. Chandrasena, W. Yang, Q. Lei, M. U. Delgado-Jaime, K. D. Wijesekara, M. Golalikhani, B. A. Davidson, E. Arenholz, K. Kobayashi, M. Kobata, F. M. F. de Groot, U. Aschauer, N.A. Spaldin, X. X. Xi, and A. X. Gray, *Nano Lett.* **17**, 794 (2017).
- [22] I. C. Tung, I-Cheng Tung, G. Luo, J. H. Lee, S. H. Chang, J. Moyer, H. Hong, M. J. Bedzyk, H. Zhou, D. Morgan, D. D. Fong, and J. W. Freeland, *Phys. Rev. Materials* **1**, 053404 (2017).

- [23] M. Anada, K. Kowa, H. Maeda, E. Sakai, M. Kitamura, H. Kumigashira, O. Sakata, Y. Nakanishi-Ohno, M. Okada, T. Kimura, and Y. Wakabayashi, Phys. Rev. B **98**, 014105 (2018).
- [24] M. Golalikhani, Q. Lei, R. U. Chandrasena, L. Kasaei, H. Park, J. Bai, P. Orgiani, J. Ciston, G. E. Sterbinsky, D. A. Arena, P. Shafer, E. Arenholz, B. A. Davidson, A. J. Millis, A. X. Gray, and X. X. Xi, Nat. Commun. **9**, 2206 (2018).
- [25] B. R. K. Nanda, S. Satpathy, and M. S. Springborg, Phys. Rev. Lett. **98**, 216804 (2007).
- [26] A. T. Young, E. Arenholz, J. Feng, H. Padmore, S. Marks, R. Schlueter, E. Hoyer, N. Kelez, and C. Steier, Surf. Rev. Lett. **09**, 549 (2002).
- [27] S. Middey, D. Meyers, M. Kareev, E. J. Moon, B. A. Gray, X. Liu, J. Freeland, and J. Chakhalian, **101**, 261602 (2012).
- [28] Y. Bitla, Y. Y. Chin, J. C. Lin, C. N. Van, R. Liu, Y. Zhu, H.-J. Liu, Q. Zhan, H. J. Lin, C. T. Chen, Y. H. Chu, and Q. He, Sci. Rep. **5**, 15201 (2015).
- [29] Y. Yokoyama, D. Ootsuki, T. Sugimoto, H. Wadati, J. Okabayashi, x. Yang, F. Du, G. Chen, and T. Mizokawa, Appl. Phys. Lett. **107**, 033903 (2015).
- [30] N. B. Aetukuri, A. X. Gray, M. Drouard, M. Cossale, L. Gao, A. H. Reid, R. Kukreja, H. Ohldag, C. A. Jenkins, E. Arenholz, K. P. Roche, H. A. Dürr, M. G. Samant, and S. S. P. Parkin, Nat. Phys. **9**, 661 (2013).
- [31] E. Arenholz, G. van der Laan, R. V. Chopdekar, and Y. Suzuki, Phys. Rev. B **74**, 094407 (2006).
- [32] V. N. Strocov, X. Wang, M. Shi, M. Kobayashi, J. Krempasky, C. Hess, T. Schmitt, and L. Patthey, J. Synchrotron Rad. **21**, 32 (2014).
- [33] V. N. Strocov, T. Schmitt, U. Flechsig, T. Schmidt, A. Imhof, Q. Chen, J. Raabe, R. Betemps, D. Zimoch, J. Krempasky, X. Wang, M. Grioni, A. Piazzalunga, and L. Patthey, J. Synchrotron Rad. **17**, 631 (2010).
- [34] A. X. Gray, C. Papp, B. Balke, S.-H. Yang, M. Huijben, E. Rotenberg, A. Bostwick, S. Ueda, Y. Yamashita, K. Kobayashi, E. M. Gullikson, J. B. Kortright, F. M. F. de Groot, G. Rijnders, D. H. A. Blank, R. Ramesh, and C. S. Fadley, Phys. Rev. B **82**, 205116 (2010).

- 1 [35] A. M. Kaiser, A. X. Gray, G. Conti, J. Son, A. Greer, A. Perona, A. Rattachata, A. Y.  
2 Saw, A. Bostwick, S. Yang, S.-H. Yang, E. M. Gullikson, J. B. Kortright, S. Stemmer,  
3 and C. S. Fadley, Phys. Rev. Lett. **107**, 116402 (2011).
- 4 [36] S.-H. Yang, A. X. Gray, A. M. Kaiser, B. S. Mun, B. C. Sell, J. B. Kortright, and C. S.  
5 Fadley, J. Appl. Phys. **113**, 073513 (2013).
- 6 [37] J. Chakhalian, J. M. Rondinelli, Jian Liu, B. A. Gray, M. Kareev, E. J. Moon, N. Prasai,  
7 J. L. Cohn, M. Varela, I. C. Tung, M. J. Bedzyk, S. G. Altendorf, F. Strigari, B. Dabrowski,  
8 L. H. Tjeng, P. J. Ryan, and J. W. Freeland, Phys. Rev. Lett. **107**, 116805 (2011).
- 9 [38] M. C. Weber, M. Guennou, N. Dix, D. Pesquera, F. Sánchez, G. Herranz, J.  
10 Fontcuberta, L. López-Conesa, S. Estradé, F. Peiró, Jorge Iñiguez, and J. Kreisel, Phys.  
11 Rev. B **94**, 014118 (2016).
- 12 [39] C. L. Flint, A. J. Grutter, C. A. Jenkins, E. Arenholz, and Y. Suzuki, J. Appl. Phys. **115**,  
13 17D712 (2014).
- 14 [40] See Supplemental Material at <http://link.aps.org/supplemental/xxxxx>.
- 15 [41] V. R. Galakhov, M. Demeter, S. Bartkowski, M. Neumann, N. A. Ovechkina, E. Z.  
16 Kurmaev, N. I. Lobachevskaya, Ya. M. Mukovskii, J. Mitchell, and D. L. Ederer,  
17 Phys. Rev. B **65**, 113102 (2002).
- 18 [42] E. Beyreuther, S. Grafström, L. M. Eng, C. Thiele, and K. Dörr, Phys. Rev. B **73**, 155425  
19 (2006).
- 20 [43] L. Qiao and X. Bi, Europhys. Lett. **93**, 57002 (2011).
- 21 [44] X. Ning, Z. Wang, and Z. Zhang, Sci. Rep. **5**, 8460 (2015).
- 22 [45] M. Burriel, S. Wilkins, J. P. Hill, M. A. Munoz-Marquez, H. H. Brongersma, J. A.  
23 Kilner, M. P. Ryan, and S. J. Skinner, Energy Environ. Sci. **7**, 311 (2014).
- 24 [46] A. Jablonski and C. J. Powell, J. Vac. Sci. Technol. A **27**, 253 (2009).
- 25 [47] W. Smekal, W. S. M. Werner, and C. J. Powell, Surf. Interface Anal. **37**, 1059 (2005).
- 26 [48] J. B. Goodenough, J. Phys. Chem. Solids **6**, 287 (1958).
- 27 [49] J. Kanamori, J. Phys. Chem. Solids **10**, 87 (1959).